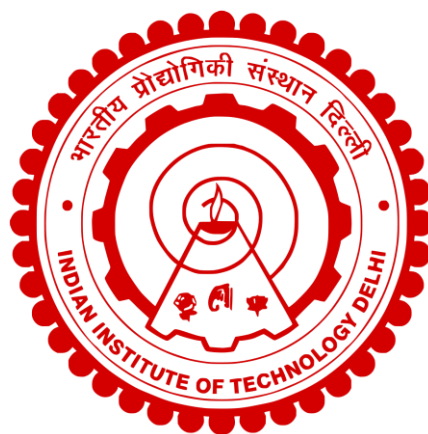


OPTIMIZING HETEROGENEOUS PHOTOCATALYST DESIGN FOR CO₂ REDUCTION TO FUELS

SHREYA SINGH



**DEPARTMENT OF CHEMICAL ENGINEERING
INDIAN INSTITUTE OF TECHNOLOGY DELHI**

JULY 2024

© Indian Institute of Technology Delhi (IITD), New Delhi, 2024

Optimizing Heterogeneous Photocatalyst Design for CO₂ Reduction to Fuels

by

SHREYA SINGH

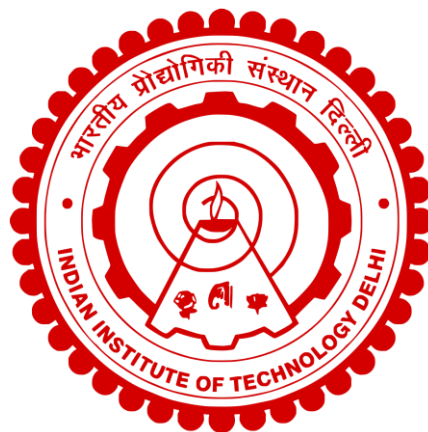
Department of Chemical Engineering

Submitted

in fulfilment of the requirement for the award of the degree of

Doctor of Philosophy

to the



INDIAN INSTITUTE OF TECHNOLOGY DELHI

JULY 2024

*To my inspiring parents
and loving husband, for
always nurturing my
curiosities...*

Certificate

This is to certify that the thesis entitled “**Optimizing Heterogeneous Photocatalyst Design for CO₂ Reduction to Fuels**” submitted by **Mrs. Shreya Singh** to the Indian Institute of Technology Delhi, for the award of degree of **Doctor of Philosophy** is a record of bonafide research work carried out by her. Mrs. Shreya Singh worked under our guidance and supervision and has fulfilled the requirements, which to my knowledge has reached the requisite standard for the submission of this thesis. The results contained in this thesis are original and have not been submitted, partially or completely, to any other University or Institute for the award of any other degree or diploma.



Prof. K. K. Pant

Professor

Department of Chemical Engineering

Indian Institute of Technology Delhi

Hauz Khas, New Delhi-110016



Prof. Anil Verma

Professor

Department of Chemical Engineering

Indian Institute of Technology Delhi

Hauz Khas, New Delhi-110016



Prof. Pratim Biswas

Professor

Chemical, Environmental and Materials Engineering

University of Miami, Coral Gables, FL 33124

Acknowledgements

First of all, I would like to express my heartfelt gratitude to my supervisor, Prof. K. K. Pant, for giving me the opportunity to work in his research group, for the freedom of research paired with continuous advertence and support, for his stimulating enthusiasm and providing me the opportunity to work on such an interesting project. He was always willing and enthusiastic to help me in any way he could throughout my research journey. It is very much appreciated that I had access to all the facilities within and outside the CRE lab just because of him, even after his transition to a new institute. Despite his quite busy schedule, he still squeezed some time to help me out. His support made all the difference and made me overcome many difficulties with such an ease. Without his professional guidance, profound knowledge, invaluable ideas, and suggestions this thesis would not have become what it is.

Also, I would like to express my sincere thanks and warm regards to my co-supervisors Prof. Pratim Biswas and Prof. Anil Verma for their cooperation, valuable help and support during my research work.

I am also thankful to Prof. Anil Kumar Saroha, Head, Department of Chemical Engineering, for providing all the necessary facilities during my work at IIT Delhi. I thank my research committee members Prof. K.A. Subramanian, Prof. Sreedevi Upadhyayula and Prof. Divesh Bhatia for their immense inspiration, valuable suggestions, correct directions, and thoughtful corrections which have been instrumental in the successful completion of my work. I appreciate their willingness to give time and guidance throughout my research, even with their busy schedules, and for always being there when I needed help. I would like to pay my special regards to Prof. M. Ali Haider, who taught me basic quantum-chemistry and software know-hows in the beginning of my research. Prof. Haider has been a great source of inspiration to me, his encouragement and endless kindness has had an immeasurable impact on my career path particularly in the domain of catalysis. I also thank all the other faculty members and office staff of the Department for being so cordial and helping me whenever necessary.

I am truly thankful to the Central Research Facility (CRF), Nano Research Facility (NRF) and High-Performance Computing (HPC) facility at IIT Delhi for providing the instrumentation and computational facilities during these years. I am indebted to Prof. B. Viswanathan for introducing

me into the brave new world of “photocatalysis”, for his encouragement to relentlessly explore deeper, his belief that time is a secondary concern compared to the pursuit of knowledge, and for his endless array of questions, answers, ideas and patience, and being my mentor in life. For opening the intriguing playground of photochemistry and shifting the focus to the most interesting problems.

My deepest gratitude to my best-friend and husband, Rajat Punia, for his invaluable counsel (both in real and in reciprocal space) and his perspective, at times challengingly unique, has opened my eyes to new dimensions in our discussions about photocatalysis and life’s myriad complexities. His unflappable ability to listen, offer clarity amidst chaos, share an inspiringly distinct view and de-dramatizing things with remarkably unique world outlook – I learned a lot. Your wisdom and guidance are the treasures I hold dear. Thank you for being a beacon of understanding and perspective in this beautiful journey.

Genuine thankfulness to my juniors, Guguloth Venkanna and Abdul Rafey, for keeping company in our “Micromodel-lab”, for being an unfailing dependable pillar throughout, and for racking their brains in proofreading this thesis and for being there always.

I also owe a huge thanks to my dear friend Jayashree Pati for her encouragement and support over the years. Her assistance in technical, scientific, and personal matters has been invaluable and a crucial part of this journey. Additionally, I extend my gratitude to my collaborators Prof. S. Satapathi, Prof. Apurba Sinhamahapatra, Prof. S. Kumar, Dr. Naveen Kumar Tailor, Dr. Smruti Purohit, Mr. Roushan Kumar, Dr. Pankaj Tiwari, Dr. Abhinav Bajpai, Dr. D. Joshi and the OpenAI team. Their collaboration, creative discussions, and consistent support have significantly eased the research process.

I must also extend a huge thank you to the many friends who were a meaningful part of this journey, a number of whom I had the fortune to meet during my Ph.D. studies. Each of you, in no specific order, as every one of you holds a special place, Ms. Snigdha Mishra, Ms. Akshata Ramteke, Dr. Uma Dwivedi, Dr. Ramdayal Panda, Dr. Komal Tripathi, Ms. Sadaf Aiman, Ms. Nidhi Kushwaha, Mrs. Shally Gupta, thanks for your supportive presence. I extend heartfelt thanks to my wonderful and supportive colleagues, both past and present, for their invaluable assistance in various areas. I'm grateful to Dr. Sonal Asthana, Dr. Ejaz Ahmad, Dr. Arindam

Modak, Dr. Kunwar Pal, Dr. Rohit Kumar, Dr. Ashish Pandey, Dr. Kaushal Parmar, Dr. Ashish Bohre, Dr. Prashant Jadhao, Dr. Rajan Singh, Dr. Dheeraj Kumar, Dr. Akshay Mankar, Dr. Vallari Chaurasia, Mr. Sagar Dhanushkar, Mr. Vaibhav Pandey, Ms. Deepti Mishra, Ms. Aisha Noor, Ms. Neethu, Mr. Pranit Samanta, Mr. Shashank Shekhar, Mr. Marut Jain, and Mr. Kaushik Kundu for their support and encouragement throughout. Additionally, I would like to express my earnest acknowledgement to Mr. Vishesh Kumar, Mr. Krishna Kumar, Mr. Gautam Kumar, Mr. Suchit Kumar, Mr. Ashish Pal, Mr. Shankar Singh, and Mr. Vijay Pal for their continuous help, ensuring the smooth progress of my research work.

Foremost, my deepest gratitude goes to my family—my parents, siblings (Varsha, Deepak and Aditya), in-laws, and my brother-in-law (Dr. Rajan) for their unwavering support and boundless patience throughout this journey. Their sacrifices and encouragement have been the bedrock of my perseverance. In the face of such profound support, words often fall short. Indeed, when the heart is brimming with gratitude, language can scarcely capture the fullness of its emotion.



Shreya Singh

Research is to see what everybody else has seen, and to think what nobody else has thought

Albert Szent-Györgyi

Abstract

As global energy demands escalate, the resultant rise in greenhouse gas emissions, particularly carbon dioxide (CO₂), has galvanized the scientific community to seek sustainable alternatives to fossil fuels. A promising research direction is the photocatalytic reduction of CO₂ to produce solar fuels, offering a dual benefit: carbon sequestration and solar energy storage in high-energy-density fuels. Photocatalytic CO₂ reduction suffers from challenges such as low utilization of low-frequency spectrum of sunlight, high charge recombination rates and lack of understanding of reaction mechanisms. The effectiveness of this process relies heavily on the design of photocatalysts, which are crucial for efficiently harnessing solar energy for CO₂ reduction. This thesis presents a methodical approach to photocatalyst development, emphasizing the synthesis of materials with specific properties that enhance photon interaction, charge relaxation, and reaction activation potential, thereby boosting CO₂ conversion into solar fuels. Our research tackles two main challenges in photocatalysis: low light-utilization efficiency and charge recombination losses. We employ principles of rational design, such as heterojunctions (MoS₂-Cu₂O) to reduce charge recombination and improve redox potential, transition metal doping (M-TiO₂) to understand the effect of metal doping on governing the selectivity of products and investigating metastable states of Melon carbon nitride using computational and experimental approaches and role of conformations on the photocatalytic activity. In-situ IR measurements and density functional theory calculations were used to dissect the photocatalytic reaction mechanism, identifying crucial design factors that predominantly influence a system's activity. By analysing charge relaxation and reaction rates, we propose a reaction kinetics model that accounts for charge carriers concentration and elucidates the impact of various design elements at the elementary reaction level. This model guides the molecular-level strategic modifications of photocatalysts, paving the way for more efficient solar fuel production.

सार

वैश्विक ऊर्जा की मांगों में वृद्धि के साथ, ग्रीनहाउस गैसों के उत्सर्जन, विशेषकर कार्बन डाइऑक्साइड (CO_2) में बढ़ोतरी, ने वैज्ञानिक समुदाय को जीवाश्म ईंधन के स्थायी विकल्पों की तलाश करने के लिए प्रेरित किया है। एक आशाजनक शोध दिशा CO_2 का फोटोकैटालिटिक कमीकरण है जिससे सौर ईंधन का उत्पादन होता है, जिससे दोहरा लाभ होता है: कार्बन संग्रहण और सौर ऊर्जा का उच्च-ऊर्जा-घनत्व ईंधन में भंडारण। फोटोकैटालिटिक CO_2 कमीकरण में चुनौतियां जैसे कम-आवृत्ति स्पेक्ट्रम की सूर्य की रोशनी का निम्न उपयोग, उच्च चार्ज पुनःसंयोजन दरें और प्रतिक्रिया तंत्र की समझ की कमी शामिल हैं। इस प्रक्रिया की प्रभावशीलता मुख्य रूप से फोटोकैटालिस्ट के डिजाइन पर निर्भर करती है, जो CO_2 कमीकरण के लिए सौर ऊर्जा को कुशलतापूर्वक हासिल करने के लिए महत्वपूर्ण हैं। यह थीसिस फोटोकैटालिस्ट विकास के लिए एक विधिवत दृष्टिकोण प्रस्तुत करती है, जिसमें विशिष्ट गुणों वाले सामग्रियों के संश्लेषण पर जोर दिया गया है जो फोटॉन इंटरैक्शन, चार्ज रिलैक्सेशन, और प्रतिक्रिया सक्रियण क्षमता को बढ़ाते हैं, इस प्रकार CO_2 के सौर ईंधन में रूपांतरण को बढ़ावा देते हैं। हमारा शोध फोटोकैटालिसिस में दो मुख्य चुनौतियों से निपटता है: कम प्रकाश-उपयोग दक्षता और चार्ज पुनःसंयोजन हानियां। हमने तर्कसंगत डिजाइन के सिद्धांतों का उपयोग किया, जैसे कि हेटरोजंक्शन ($\text{MoS}_2\text{-Cu}_2\text{O}$) चार्ज पुनःसंयोजन को कम करने और रेडॉक्स क्षमता में सुधार करने के लिए, धातु डोपिंग (M-TiO_2) का उपयोग करके उत्पादों की चयनात्मकता पर धातु डोपिंग के प्रभाव को समझने के लिए, और मेलन कार्बन नाइट्राइड की मेटास्टेबल स्थितियों का पता लगाने के लिए कंप्यूटेशनल और प्रयोगात्मक दृष्टिकोण और फोटोकैटालिटिक गतिविधि पर संरचनाओं की भूमिका। इन-सिटू IR माप और घनत्व कार्यात्मक सिद्धांत गणनाओं का उपयोग करके फोटोकैटालिटिक प्रतिक्रिया तंत्र की विश्लेषण किया गया, जिससे प्रणाली की गतिविधि को प्रमुख रूप से प्रभावित करने वाले डिजाइन कारकों की पहचान की गई। चार्ज रिलैक्सेशन और प्रतिक्रिया दरों का विश्लेषण करके, हमने एक प्रतिक्रिया गतिविज्ञान मॉडल का प्रस्ताव किया जो चार्ज वाहकों की एकाग्रता के लिए खाता बनाता है और मौलिक प्रतिक्रिया स्तर पर विभिन्न डिजाइन तत्वों के प्रभाव को स्पष्ट करता है। यह मॉडल फोटोकैटालिस्ट्स के मोलेक्युलर-स्तर के सामरिक संशोधनों को निर्देशित करता है, जिससे सौर ईंधन उत्पादन के लिए अधिक कुशल मार्ग प्रशस्त होता है।

Table of Contents

| | |
|---|-------------|
| Certificate | iii |
| Acknowledgements | iv |
| Abstract..... | viii |
| Table of Contents | x |
| List of Figures..... | xii |
| List of Tables | xvii |
| Chapter 1 - Introduction | 1 |
| 1.1 Overview of the current issue and related solution | 1 |
| 1.2 Photocatalytic CO ₂ Embedding into Products | 4 |
| 1.3 Choice of catalysts and need for modifications in the catalysts..... | 6 |
| 1.4 Reaction Mechanism in CO ₂ photo-reduction Process | 10 |
| 1.5 Kinetic Considerations and Controlling Parameters | 12 |
| 1.6 Limitations in scale up | 20 |
| 1.7 Summary | 20 |
| 1.8 Gaps and motivation for present work | 21 |
| 1.9 Thesis objectives | 22 |
| 1.10 Structure of thesis | 24 |
| Chapter 2 - Material and Methods..... | 26 |
| 2.1 Abstract | 26 |
| 2.2 Catalyst Synthesis | 26 |
| 2.3 Characterization Methods | 30 |
| 2.4 Reaction vessel and reaction conditions | 45 |
| 2.5 Photo-deposition experiment | 50 |
| 2.6 In-situ DRIFTS study..... | 50 |
| 2.7 Computational Methods..... | 51 |
| Chapter 3 - Mechanistic Exploration in Controlling the Product Selectivity via Metals in TiO₂ for Photocatalytic Carbon Dioxide Reduction | 60 |
| 3.1 Abstract | 60 |
| 3.2 Introduction..... | 60 |
| 3.3 Results and discussion | 64 |
| 3.4 Discussion | 92 |
| 3.5 Research significance..... | 93 |

| | |
|---|------------|
| Chapter 4 - Effect of work-function and morphology of heterostructure components on CO₂ reduction photo-catalytic activity of MoS₂-Cu₂O heterostructure | 95 |
| 4.1 Abstract | 95 |
| 4.2 Introduction..... | 95 |
| 4.3 Results and discussions..... | 106 |
| 4.4 Research significance..... | 134 |
| Chapter 5 - Carbon-Nitride Polymorphs: Unveiling the Correlation between Synthesis-Induced Structural Variations, Electronic Properties, and CO₂ Photocatalytic Activity | 136 |
| 5.1 Abstract | 136 |
| 5.2 Introduction..... | 136 |
| 5.3 Results and Discussions | 147 |
| 5.4 Research significance..... | 175 |
| Chapter 6 - The cooperative role of nitrogen defects and cyano-group functionalization in carbon nitride towards enhancing its CO₂ photoreduction activity | 176 |
| 6.1 Abstract | 176 |
| 6.2 Introduction..... | 176 |
| 6.3 Results & Discussion | 179 |
| 6.4 Research significance..... | 200 |
| Chapter 7 - Conclusion and Future Recommendations | 201 |
| 7.1 Conclusions..... | 201 |
| 7.2 Future recommendations..... | 205 |
| References..... | 207 |
| Appendix..... | i |
| Publications | iv |
| Curriculum Vitae | |

List of Figures

| | |
|---|----|
| Figure 1.1: (A) Country-wise emissions and fractions of the source contributing in emissions (Yang et al. 2022) (B) Emission scenarios of CO ₂ up to 2100 (Quere et al. 2016) | 2 |
| Figure 1.2: (Left) Band gap energies of different Semiconductors with their respective band edges. (Right) Photo-excitation of electrons from valance to conduction bands for corresponding oxidation and reduction reactions (Singh et al. 2021) | 6 |
| Figure 1.3: Different classes of photocatalyst utilized for the CO ₂ conversion process | 7 |
| Figure 1.4: Different proposed photocatalytic CO ₂ reduction pathways: (a) Formaldehyde pathway 1 electron 1 proton (b) Carbene pathway (c) Glyoxal pathway (Singh et al. 2021) | 10 |
| Figure 1.5: Kinetic parameters dependence of photocatalytic reactions (Singh et al. 2021) | 13 |
| Figure 1.6: Schematic for the overall objective of the current thesis work with utilized techniques and domains | 23 |
| Figure 2.1: Different steps of formation of pristine and different M-TiO ₂ | 27 |
| Figure 2.2: Variation of colour in different steps in Cu ₂ O of different morphologies | 28 |
| Figure 2.3: Synthesized carbon nitride materials from melamine at different temperatures | 29 |
| Figure 2.4: Formation steps of cyano functionalization in carbon nitride structure | 30 |
| Figure 2.5: Schematic of different types of properties for photocatalyst characterization | 30 |
| Figure 2.6: Schematic of annular quartz reactor with inside light illumination | 46 |
| Figure 2.7: Picture of the experimental setup of the stainless steel and photoreactor setup with top illumination | 47 |
| Figure 2.8: (A) Controlled experiments for confirmation of the CO ₂ photocatalytic reduction with carbon nitride catalyst (B) Mass spectrum of photocatalytic products generated during Isotopic ¹³ CO ₂ labelled photoreduction experiment over Carbon nitride photocatalyst | 49 |
| Figure 2.9: Schematic of in-situ FTIR, with DRIFTS cell of the HARRICK praying Mantis reaction chamber in Nicolet is50 (Manufacturer: Thermo Fisher scientific) | 50 |
| Figure 2.10: Wavefunction and Potential Analysis: Real versus Pseudopotential Beyond Crossover Radius | 54 |
| Figure 2.11: Calculation Model for heterojunctions of MoS ₂ (002) facet and Cu ₂ O with (100) and (111) facets | 57 |
| Figure 2.12: DFT models for (A) Melon, (B) C≡N-Melon and (C) C≡N-N _v -Melon | 58 |
| Figure 3.1: XRD patterns for TiO ₂ and P25 nanocrystals with marked diffraction peaks corresponding to the anatase and rutile phases of TiO ₂ | 65 |
| Figure 3.2: XRD patterns for different M-TiO ₂ (M=Ag, Cu, Au) nanocrystals with varied metal loading amounts | 65 |
| Figure 3.3: Narrow range XRD pattern to observe the shifts in the diffraction peaks corresponding to the 101 planes of M-TiO ₂ (M=Ag, Cu, Au) | 67 |
| Figure 3.4: Raman spectra of TiO ₂ doped with Cu, Au, and Ag (from left to right) at concentrations from 0.1 to 1 wt% of metal dopant | 67 |
| Figure 3.5: Narrow range Raman spectra of TiO ₂ doped with Cu, Au, and Ag (from left to right) at concentrations from 0.1 to 1 wt% of metal dopant | 68 |
| Figure 3.6: Thermogravimetric analysis (A) and nitrogen adsorption isotherms (B) of TiO ₂ doped with Au, Ag, and Cu, showing thermal stability and porosity characteristics, respectively | 69 |
| Figure 3.7: Particle size distribution profile for (A) Cu (B) Au and (C) Ag based TiO ₂ samples | 71 |

| | |
|---|-----|
| Figure 3.8: Transmission electron microscopy images of Au/TiO ₂ nanoparticles: (A) low magnification, (B) high-resolution with inset showing selected area electron diffraction pattern, and (C) corresponding elemental mapping for O, Ti, and Au | 72 |
| Figure 3.9: Transmission electron microscopy images of Ag/TiO ₂ nanoparticles: (A) low magnification, (B) high-resolution with inset showing selected area electron diffraction pattern, and (C) corresponding elemental mapping for O, Ti, and Ag | 72 |
| Figure 3.10: Transmission electron microscopy images of Cu/TiO ₂ nanoparticles: (A) low magnification, (B) high-resolution with inset showing selected area electron diffraction pattern, and (C) corresponding elemental mapping for O, Ti, and Cu | 73 |
| Figure 3.11: Narrow Scan X-ray photoelectron spectroscopy (XPS) spectra showing the binding energy shifts for (A) Ti 2p, (B) O 1s, (C) Ag 3d, (D) Au 4f, and (E) Cu 2p in pure TiO ₂ and metal-doped TiO ₂ (Cu, Au, Ag) catalyst | 75 |
| Figure 3.12: Temperature-programmed reduction (TPR) profiles of pure TiO ₂ and metal-doped TiO ₂ catalysts: (A) TiO ₂ , (B) Cu-TiO ₂ , (C) Ag-TiO ₂ , and (D) Au-TiO ₂ | 76 |
| Figure 3.13: UV-Vis absorption spectra of TiO ₂ and metal-doped TiO ₂ catalysts with varying metal loadings: Ag-TiO ₂ (left), Au-TiO ₂ (centre), Cu-TiO ₂ (right) | 78 |
| Figure 3.14: Photoluminescence spectra (A) and time-resolved decay curves (B) of pure TiO ₂ and metal-doped TiO ₂ (Ag, Au, Cu) catalysts | 79 |
| Figure 3.15: Electrochemical impedance spectroscopy (EIS) Nyquist plots (A) and linear sweep voltammograms (B) for pure TiO ₂ and metal doped TiO ₂ (Ag, Au, Cu) under dark ('d') and light ('l') conditions | 81 |
| Figure 3.16: Kelvin Probe Force Microscopy (KPFM) potential mapping of pure TiO ₂ (A), and metal-doped TiO ₂ : Cu-TiO ₂ (B), Au-TiO ₂ (C), Ag-TiO ₂ (D) | 82 |
| Figure 3.17: Ultraviolet photoelectron spectroscopy (UPS) spectra showing valence band maxima for TiO ₂ , and metal doped TiO ₂ with copper (Cu), gold (Au), and silver (Ag) | 83 |
| Figure 3.18: Photocatalytic activity profiles for M-TiO ₂ (M= Cu, Au, Ag) towards CH ₄ , CO CH ₃ OH and H ₂ generation | 84 |
| Figure 3.19: Electron Selectivity comparison for HER or CO ₂ RR for different metal loadings in M-TiO ₂ (M= Cu, Au, Ag) | 86 |
| Figure 3.20: CO ₂ Temperature programmed desorption profiles at different ramp rates to evaluate the BE of different metals for M-TiO ₂ (M= Cu, Au, Ag) | 86 |
| Figure 3.21: The time-resolved DRIFT spectra of (A) Cu (B) Au and (C) Ag incorporated TiO ₂ on adsorbing CO ₂ /H ₂ O at 30 °C under dark | 88 |
| Figure 3.22: The time-resolved DRIFT spectra of (A) Au (B) Ag and (C) Cu incorporated TiO ₂ after light-on with corresponding peak assignments | 90 |
| Figure 3.23: CO temperature programmed desorption profile for Ag and Cu-TiO ₂ | 91 |
| Figure 3.24: The scheme of plausible reaction pathway for CO, CH ₄ , CH ₃ OH production with boxed intermediates in green and pink demonstrating the stabilization over Cu and Ag surfaces | 93 |
| Figure 4.1: Alterations in the band edge potentials of wide gap semiconductor photocatalyst in the process of enhancing light absorption ability | 96 |
| Figure 4.2: Semiconductor coupling modes (A) type II heterojunction (B) direct z-scheme PC1 and PC2 stand for the conduction band, valence band, photocatalyst I and photocatalyst II, respectively | 98 |
| Figure 4.3: Field emission scanning electron microscopic images of (A) p-MoS ₂ (B) n-MoS ₂ (C) Cu ₂ O-cubic (D) Cu ₂ O-cubo-octahedrons (E) n-MoS ₂ -Cu ₂ O-c (F) p-MoS ₂ -Cu ₂ O-co (G) EDS mapping of p-MoS ₂ -Cu ₂ O-c composite with mapped individual elements G(b-e) | 107 |

| | |
|---|-----|
| Figure 4.4: (A) HR-TEM image of Cu ₂ O-c over p-MoS ₂ (B) SAED Patterns of Cu ₂ O-c over p-MoS ₂ marked with the fringe spacings of MoS ₂ in red, Cu ₂ O in yellow (C) HR-TEM image of Cu ₂ O-co over n-MoS ₂ (D) SAED Patterns marked with the fringe spacings of MoS ₂ in red, Cu ₂ O in yellow | 108 |
| Figure 4.5: (A) HR-TEM image and (B) SAED pattern of n-MoS ₂ (C) HR-TEM image and (D) SAED pattern for p-MoS ₂ | 109 |
| Figure 4.6: XRD spectra of different individual (MoS ₂ and Cu ₂ O) and their heterostructures | 110 |
| Figure 4.7: (A) Raman scattering spectra of p-MoS ₂ and n-MoS ₂ (B) High resolution X-ray photoelectron spectroscopy of S atom (left) and Mo atom (right) in p-MoS ₂ (bottom) and n-MoS ₂ (top) | 112 |
| Figure 4.8: Normalized room temperature EPR spectra of n-MoS ₂ (red line) and the p-MoS ₂ (black line) | 114 |
| Figure 4.9: CO ₂ temperature programmed desorption (CO ₂ -TPD) spectra for Cu ₂ O cubic (blue, bottom) cubo-octahedrons (black, top) (B) CO ₂ binding mode on {111} and {100} facets of Cu ₂ O | 115 |
| Figure 4.10: GCMS spectra of the liquid product sample obtained after photocatalytic reaction with p-MoS ₂ -Cu ₂ O-c catalysts with TEOA as the sacrificial agent | 116 |
| Figure 4.11: Photocatalytic activity of heterostructures. Methanol yield in batch mode in 4 h (A) With different catalyst loading of Cu ₂ O-co (B) for different photocatalysts and their heterostructures in absence of Sacrificial agent (TEOA) (C) for different photocatalysts and their heterostructures in presence of Sacrificial agent (TEOA) (D) Cyclic experiments for stability of the best performing heterostructure photocatalyst i.e. p-MoS ₂ -Cu ₂ O-c | 118 |
| Figure 4.12: XRD of the spent catalyst (black) in comparison to the fresh catalyst of p-MoS ₂ -Cu ₂ O-c catalyst | 121 |
| Figure 4.13: FE-SEM and EDS mapping of the used p-MoS ₂ -Cu ₂ O-c catalyst | 121 |
| Figure 4.14: (A and B) Mott–Schottky (MS) plot of n-MoS ₂ and p-MoS ₂ (solid, black) along with the line fitted in the linear region of MS plot (dotted, red) (C) Linear sweep voltammetry (LSV) curves of individual photocatalysts (dotted lines) and heterostructures (solid lines) (D) Electrochemical impedance spectroscopy (EIS) Nyquist plots of all photocatalysts and equivalent circuit used to fit the shown data | 123 |
| Figure 4.15: Mott-Schottky Curve for (left) Cu ₂ O-c (right) Cu ₂ O-co | 124 |
| Figure 4.16: Band structures for MoS ₂ , Cu ₂ O and their heterostructure | 126 |
| Figure 4.17: Diffuse reflectance UV–Vis absorbance spectra of all photocatalysts in the wavelength range of 200–800 nm (Inset: Tauc’s plots for Cu ₂ O-c (black) and Cu ₂ O-co (red)). | 127 |
| Figure 4.18: Partial density of states (PDOS) of MoS ₂ without any change in d-spacing (B) with increased d-spacing (C) with increased d-spacing and oxygen incorporation | 128 |
| Figure 4.19: Partial Density of States for (A) Cu ₂ O-co (B) Cu ₂ O-c | 129 |
| Figure 4.20: Full-Survey XPS spectrum for different MoS ₂ and Cu ₂ O Heterostructures | 132 |
| Figure 4.21: High resolution XPS spectra of Mo 3d and Cu 2p in (A) p-MoS ₂ -Cu ₂ O-c (B) n-MoS ₂ -Cu ₂ O-c (C) Direction of migration of electrons and holes upon heterostructure formation and band bending in p-MoS ₂ and p-MoS ₂ -based heterostructures (D) Photo-deposition of Pt over Cu ₂ O in p-MoS ₂ -Cu ₂ O-c heterojunction catalyst (left) and zoomed image along with the SAED pattern (right) | 134 |
| Figure 5.1: Several structural forms of carbon nitride possible from basic building blocks | 137 |
| Figure 5.2: Synthetic routes for the formation of carbon and nitrogen-based molecules and advanced carbon nitride frameworks (reproduced with permission from Lau and Lotsch 2022) | 138 |
| Figure 5.3: Planar structure of melon as proposed by Lotsch et. al reproduced after permission from (Lotsch et al. 2007) | 141 |
| Figure 5.4: Clustering of different so obtained structural geometries based on RMSD <0.5Å | 149 |
| Figure 5.5: (A) Solid-state ¹³ C NMR of CN-500 with inset ¹ H and (B) FTIR spectra of carbon nitride materials synthesized at temperatures ranging from 500 to 650°C | 151 |

| | |
|---|-----|
| Figure 5.6: (A) XRD patterns and (B) Raman spectra of carbon nitride synthesized at different temperatures (500, 550, 600, and 650°C) with peak shift corresponding to 002 plane (inset of A) and crystallinity changes | 153 |
| Figure 5.7: (A) SEM images (B) elemental mapping (C) particle size distribution, and (D) HR-TEM images with SAED patterns of carbon nitride synthesized at different temperatures | 155 |
| Figure 5.8: Narrow range XPS Spectra for carbon nitride samples (A) N1s and (B) C1s elements | 157 |
| Figure 5.9: Photocatalytic activity test product yield for different carbon nitride samples | 159 |
| Figure 5.10: (A) UV-Vis absorption spectra, (B) photoluminescence spectra, (C) VB-XPS spectra, and (D) Band edge potential for different CN-T samples | 160 |
| Figure 5.11: (A) nitrogen adsorption-desorption isotherms with pore size distribution inset, (B) electrochemical impedance spectroscopy, (C) linear sweep voltammetry profiles of CN-T samples (D) surface potential distribution, and (E, F) Kelvin probe force microscopy (KPFM) under light-off and light-on conditions, respectively | 163 |
| Figure 5.12: (A) CO ₂ Temperature programmed desorption profile for different CN-T samples, (B) Equation fit profile for CN-500, (C) Binding energy for different CN-T samples | 165 |
| Figure 5.13: EPR Profile (A) without and (B) with light irradiation and decay profile of time resolved luminescence spectra for different CN-T samples | 166 |
| Figure 5.14: Experimental and fitted photoreduction data for CO and CH ₄ over carbon nitride synthesized at varying temperatures | 171 |
| Figure 5.15: Experimental and fitted photoreduction data for CO and CH ₄ over CN-500 synthesized at varying sacrificial agent concentrations | 174 |
| Figure 6.1: Overview of synthesis process for cyano (C≡N) rich Nitrogen vacant (N _v) carbon nitride | 179 |
| Figure 6.2: (A and B) XRD spectra and IR spectra of CN, CN-300-N ₂ , CN-300-air, CN-400-N ₂ , CN-400-air, CN-500-N ₂ and CN-500-air. (C) High-resolution N 1s XPS spectra of CN and CN-400-air. (D) High-resolution C 1s XPS spectra of CN and CN-400-air | 182 |
| Figure 6.3: (A) FTIR Spectra for different reheated and modified carbon nitride samples; (B) Narrow scan spectra for O1s in CN-400-air sample (C) Narrow scan spectra for C1s and N 1s in CN-500-air and CN-500-N ₂ samples | 184 |
| Figure 6.4: (A) FESEM (top) and HRTEM (bottom) images with inset representing the corresponding selected area electron diffraction (SAED) pattern of pristine (CN) and modified carbon nitride (CN-400-air); (B) N ₂ adsorption-desorption isotherms with Pore-size distribution (inset) | 186 |
| Figure 6.5: (A) Histogram for particle size distribution for CN-400-air sample (B) Elemental mapping and distribution for CN-400-air | 187 |
| Figure 6.6: Catalytic performance (yield) towards photocatalytic CO ₂ reduction in presence of TEOA to (A) CH ₄ (B) CO (C) Selectivity of synthesized photocatalysts. (D) Recyclability test result for CN-400-air | 190 |
| Figure 6.7: Catalytic performance (yield) in absence of sacrificial agent (TEOA) towards photocatalytic CO ₂ reduction to (A) CO and CH ₄ (B) Selectivity towards generated C products for different synthesized photocatalyst samples | 190 |
| Figure 6.8: (A) UV-visible diffusion reflectance absorption spectra for all the prepared catalysts (B) Surface potential distribution of CN and CN-400-air relative to the tip, obtained from kelvin probe force microscopy (KPFM) (C) Steady state photoluminescence (PL) spectra (D) Time-resolved PL decay spectra of pristine and CN-400-air | 191 |
| Figure 6.9: Calculated PDOS for different models of carbon nitride s (red), p (blue) and total (black) contribution of energy | 192 |
| Figure 6.10: Band structure profile for CN (left) and CN-C≡N-N _v (right) | 194 |
| Figure 6.11: (A) Linear sweep voltammetry (LSV) for transient cathodic photocurrent response under dark (dotted) and light for all materials (B) Electrochemical impedance spectroscopy (EIS) Nyquist plots and | |

equivalent circuit (inset) (C) Mott–Schottky plots of CN and CN-T-env samples. (D) Electron paramagnetic resonance (EPR) spectrum under dark and light-irradiated conditions (E) VB-XPS spectra of CN and CN-400-air (F) Calculated band edge positions for CN and CN-400-air on the potential scale with respect to normal hydrogen electrode (NHE). Dashed lines show the standard reduction potentials of relevant reactions. 197

List of Tables

| | |
|---|-----|
| Table 1.1: Various catalytic approaches for CO ₂ conversion | 3 |
| Table 1.2: Standard Redox Potentials for CO ₂ Reduction Reactions (Equation 1.2-1.9) at P=1.0 atm and T=25°C (Singh et al. 2021) | 7 |
| Table 1.3: Different modification strategies of photocatalyst materials with their advantages and disadvantages | 9 |
| Table 3.1: Overview of Diverse Catalytic Systems Utilized in CO ₂ Photoreduction Processes | 62 |
| Table 3.2: Pore characterization of TiO ₂ and metal doped TiO ₂ catalysts: total pore volume, micropore volume (V _m), BET surface area (S _{a,BET}), and mean pore diameter | 70 |
| Table 3.3: Relative population of different types of oxygens present in M-TiO ₂ as obtained from XPS O1s spectra | 75 |
| Table 3.4: Triexponential decay parameters for pure TiO ₂ and metal-doped TiO ₂ (Cu, Ag, Au) catalysts: time constants (τ) and amplitudes (A) | 80 |
| Table 3.5: Comparison of binding energies (BE) of CO ₂ and contact angles for metal-doped TiO ₂ catalysts: copper (Cu), gold (Au), and silver (Ag) | 87 |
| Table 4.1: A comparative study among MoS ₂ -based materials for photocatalytic CO ₂ reduction | 104 |
| Table 4.2: BET Surface Area Analysis for different individual component catalysts | 106 |
| Table 4.3: Atomic ratio of elements through CHNS Analysis | 112 |
| Table 4.4: Comparison of methanol productivity for p-MoS ₂ -Cu ₂ O-c and reported photocatalysts in the past few years | 119 |
| Table 4.5: Resistances obtained for different catalyst components and their hetero-structures in the equivalent circuit fit of the EIS Nyquist plots | 124 |
| Table 4.6: Calculated effective electron hole masses obtained through the parabolic fitting of conduction band minima and valance band maxima | 127 |
| Table 4.7: Fermi level determination through experimental and theoretical calculations with respect to vacuum | 131 |
| Table 5.1: Lattice parameters and ΔG values of the identified different carbon nitride polymorphs | 149 |
| Table 5.2: Variations in different kinetic parameters for different catalyst samples of carbon nitride synthesized at different temperatures | 172 |
| Table 5.3: Variations of different kinetic parameters with changing electron donor concentrations | 173 |
| Table 6.1: XPS surface ratio for C/N over prepared samples | 183 |
| Table 6.2: Element analysis for different modified carbon nitride materials | 185 |
| Table 6.3: Comparison of CO ₂ reduction rates of CN-C≡N-N _v with reported modified carbon nitride | 188 |
| Table 6.4: DFT calculated energy gaps and fermi levels for different models | 193 |
| Table 6.5: Comparative table for the DFT calculated effective masses of electrons and holes, and fermi levels for CN (Model 1) and CN-N _v -C≡N (Model 4) | 196 |
| Table 6.6: Solution resistance (R _s), charge transfer resistance (R _{ct}), Constant phase element (CPE) and flat band potential (V _{fb}) of all synthesized materials | 199 |